Research papers

Bayesian parameter identification in electrochemical model for lithium-ion batteries

Seongyoon Kim[1], Sanghyun Kim[1], Yun Young Choi, Jung-Il Choi [*]

School of Mathematics and Computing (Computational Science and Engineering), Yonsei University, Seoul 03722, Republic of Korea

ARTICLE INFO

ABSTRACT

Electrochemical models can characterize the internal behavior of cells and are powerful and effective tools for the design and management of batteries. This study proposes a comprehensive framework of Bayesian parameter identification to determine the parameter distributions in the electrochemical model and to estimate the global sensitivity of the parameters for lithium-ion batteries. Bayesian inference in parameter identification can simultaneously determine accurate parameter estimates and parameter identifiability, given specific voltage measurements. Among the several parameters in the pseudo-two-dimensional model, 15 parameters are selected to estimate the posterior distributions. The reconstructed voltage curves through the estimated parameter distributions are consistent with the reference voltages, with relative errors of less than 0.7% at various discharge rates. Changes in the parameter distributions and identifiability were investigated for different discharge rates through the estimated joint and marginal distributions of the parameters. Moreover, based on variance-based global sensitivity analysis, the identifiability of the electrochemical parameters according to the discharge rates is quantitatively analyzed. We demonstrate that the Bayesian parameter identification simultaneously obtains the parameter distributions and identifiability, considering the correlation between various parameters. The proposed framework can help to analyze the behaviors of batteries according to specific operating conditions and materials.

1. Introduction

Lithium-ion batteries (LIBs) are prominent energy storage solutions that have been implemented in various applications. Their high energy density, long lifespan, and low self-discharge make them suitable for applications in electric vehicles and energy storage systems [1,2]. Nevertheless, battery design optimization, fast charging, thermal management, cell and module optimization, and safety are ongoing challenges in LIB research [3–5]. Solutions to these issues depend on the appropriate monitoring, diagnosis, and prognosis of the internal states of the battery [6,7]. The internal states, such as the state of charge (SOC), state of health (SOH), and internal resistance, cannot be directly observed but must be inferred from measured data. However, the internal states and the nonlinear relationships between measurements and internal states originating from the multi-physics and multiscale characteristics of LIBs present weak observability. Therefore, electrochemical models, especially the pseudo-two-dimensional (P2D) model [8], have been widely applied to identify the electrochemical properties of LIBs [9–12].

Accurate measurement of the model parameters is important for developing an electrochemical model for the reliability and robustness of the LIB model, especially as the number of model parameters increases [13]. In general, some model parameters can be directly measured through additional experiments or calibrations for specific LIBs. However, these approaches require high experimental costs because the distinct types of LIBs may have different model parameters depending on various components, designs, degradation, and even manufacturing processes. Alternatively, one may consider utilizing the charge and discharge data to identify the electrochemical parameters. Parameter identification (PI) has been widely used in parallel with experimental characterization to obtain parameters that cannot be readily measured [11,14–17]. Nevertheless, the main difficulty is that PI tends to be ill-posed because usually there are no exact solutions in the form of parameters for which the corresponding model predictions exactly match the measurements [18]. To solve this issue, several approaches have been studied to improve the practical identifiability of electrochemical parameters. Khalik et al. [11] reparametrized the P2D model by normalizing and grouping parameters based on a sensitivity

analysis. This approach enabled the reduction of computational complexity and promoted the identifiability of the model parameters. Choi et al. [15] employed an identifiability analysis to select the optimal subset of P2D model parameters using the Fisher information matrix, which allowed for better identification of the critical parameters and improved the overall model accuracy. Li et al. [16] devised a multi-step parameter identification procedure to enhance the identifiability and minimize identification errors. By breaking the identification process into stages, their approach allowed for more accurate and efficient parameter estimation. Xu et al. [17] classified P2D model parameters into three types according to their sensitivities under different current conditions. The categorization facilitated the identification of the most influential parameters, which could then be prioritized in the estimation process. Chun et al. [19] utilized reinforcement learning to estimate the stoichiometric range of LIBs and determined an appropriate current input profile to boost identifiability. However, a common limitation among these methods is the necessity for preprocessing steps such as grouping, identifiability analysis, or sensitivity analysis before performing parameter identification. The additional steps can introduce complexity, increase computation time, and potentially influence the accuracy and reliability of the identified parameters.

As the PI procedure is an inverse problem, it typically admits many approximate solutions, where the model predictions corresponding to the estimated parameters match the measurements only approximately [20]. Uncertainty quantification (UQ) for the PI in an electrochemical model can be conveniently characterized in the framework of Bayesian inference, in which unknown parameters are inferred in terms of their probability distributions [21–23]. The Markov chain Monte Carlo (MCMC) algorithm, a strategy for generating samples from complex high-dimensional distributions, is usually used to estimate the distributions of electrochemical parameters [24,25]. The basis of MCMC is to construct stationary chains of samples; the posterior probability is the invariant distribution of the Markov chain [26]. Most studies have used MCMC on the electrochemical model to estimate the distributions of a few selected parameters or utilized a surrogate model that may cause model errors. Nevertheless, examining the distribution behaviors of various electrochemical parameters of the complete P2D model can help analyze the internal states of batteries according to the specific operating conditions and materials.

This study proposes a comprehensive framework of Bayesian PI to determine the parameter distribution in the electrochemical model and evaluate the global sensitivity of the parameters to the voltage under the applied C-rates into the LIBs, as illustrated in Fig. 1. As Bayesian PI is based on a stochastic approach that requires significant computations, we first developed an accelerated in-house P2D model solver. Subsequently, using MCMC, posterior distributions of 15 parameters in the P2D model were estimated via constant-current discharge voltage curves under various C-rates, and the optimal parameter set was obtained to maximize the posterior distribution. The estimated parameter distributions and voltage curves were validated with reference parameters and voltages, respectively, and the distribution behaviors of individual and correlated parameters were investigated for different C-rates. Moreover, a variance-based global sensitivity analysis was performed for various C-rates to investigate the sensitivity and identifiability of electrochemical parameters. We demonstrate that the proposed framework simultaneously estimates the parameter distributions and global sensitivity without grouping, fixing, or removing parameters to improve identifiability. The contributions of this study cover the complete framework from Bayesian PI to global sensitivity analysis in the electrochemical model, which can help analyze the internal behaviors of LIBs in effectively designing and managing the battery.

The remainder of this paper is organized as follows. Section 2 presents the procedure for the Bayesian PI, sensitivity analysis, and model formulation. The implementation details are presented in Section 3, and Section 4 presents the validation of the P2D solver and the results of Bayesian PI. Section 5 presents the major conclusions drawn from this study and outlines the scope of future research.
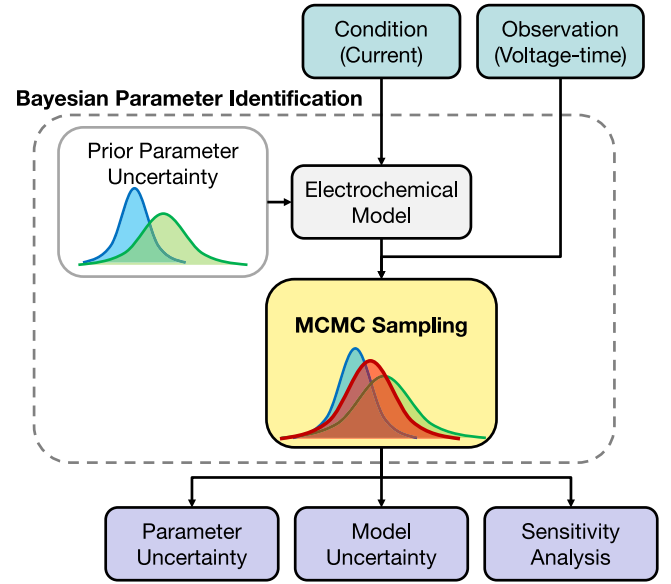

Fig. 1. Flowchart of the Bayesian parameter identification.

2. Methodology

2.1. Bayesian inference for parameter identification

Bayesian inference has been adopted in the inverse problem to estimate the distribution of input parameters using observed data. In the Bayesian framework, the posterior distribution of the parameter vector $\mathbf{x}$ conditioned on the observed data $\mathbf{y}$ can be described as follows:

$$p(\mathbf{x}|\mathbf{y}) = \frac{p(\mathbf{y}|\mathbf{x})p(\mathbf{x})}{p(\mathbf{y})}, \tag{1}$$

where $p(\mathbf{x})$ is the prior, $p(\mathbf{y}|\mathbf{x})$ is the likelihood, and $p(\mathbf{y})$ is the marginal probability density of the experimental data. The latter typically functions as a normalization factor and can be determined by

$$p(\mathbf{y}) = \int p(\mathbf{y}|\mathbf{x})p(\mathbf{x})d\mathbf{x}. \tag{2}$$

As the evaluation of high-dimensional integrals is computationally expensive, the Monte Carlo integration can be used to randomly sample from the posterior distribution. In this study, MCMC with an affine invariant ensemble sampler (AIES) [25] was adopted to accommodate the potentially strong correlation among the parameters. The AIES algorithm proposes a new candidate parameter $\mathbf{x}_i^{(*)}$, as follows:

$$\mathbf{x}_i^{(*)} = \mathbf{x}_i^{(t)} + Z(\mathbf{x}_j^{(t)} - \mathbf{x}_i^{(t)}), \text{ where } Z \sim p(z) = \begin{cases} \frac{1}{\sqrt{z}\left(2\sqrt{a} - \frac{2}{\sqrt{a}}\right)} & \text{if } z \in [1/a, a] \\ 0 & \text{otherwise,} \end{cases} \tag{3}$$

where i and j are chain indices ($i \neq j$). This requires sampling from the distribution $p(z)$ defined by the tuning parameter $a > 1$, which is often set as $a = 2$ [25]. The candidate parameter $\mathbf{x}_i^{(*)}$ is accepted with probability

$$\alpha\left(\mathbf{x}_i^{(*)}, \mathbf{x}_i^{(t)}, z\right) = \min\left\{1, z^{M-1}\frac{p(\mathbf{x}_i^{(*)}|y)}{p(\mathbf{x}_i^{(t)}|y)}\right\}, \tag{4}$$

where M denotes the dimension of the parameter space. After the iterations are completed, the resulting samples are distributed according to the posterior distribution. Finally, the maximum a posteriori (MAP) estimation is used to select the optimal parameter set from the posterior
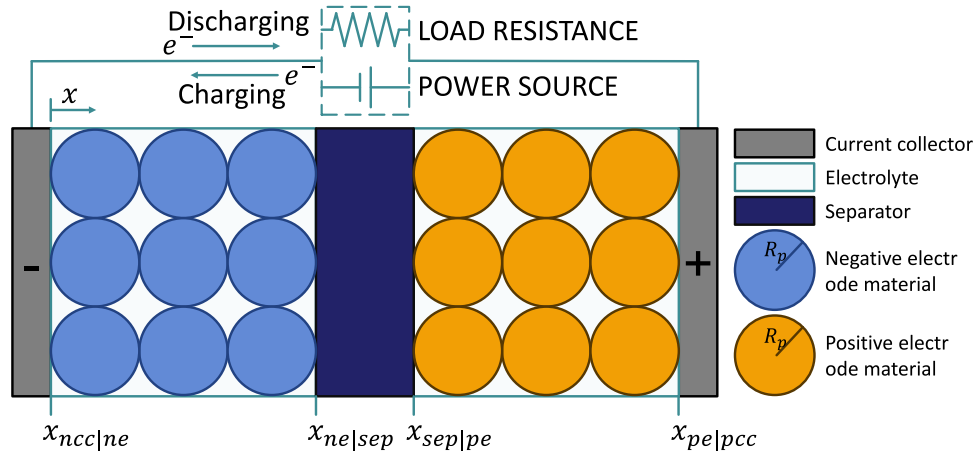
Fig. 2. Diagram of the lithium-ion battery.

parameter distributions [27], where the MAP of the parameters, $\mathbf{x}_{MAP}$, maximizes the posterior distribution function as follows:

$$\mathbf{x}_{MAP} = \arg\max_{\mathbf{x}} p(\mathbf{x}|\mathbf{y}). \qquad (5)$$

2.2. Sensitivity analysis

After obtaining the posterior distribution of the parameters in the electrochemical model, the sensitivity of the parameters to the model outputs was analyzed. Unlike local sensitivity analysis, global sensitivity analysis (GSA) aims to quantify the sensitivity of the outputs of a model to the input variables by considering the entire variation range of each input variable. In other words, the GSA examines the model behavior over the entire range of inputs and outputs. Sobol' indices are variance-based GSA methods, which are based on the expansion of the computational model into summands of increasing dimension [28]; the total variance of the model is described in terms of the sum of the variances of the summands.

Consider a model $f(\mathbf{x})$ for a D-dimensional parameter vector $\mathbf{x} = [x_1, x_2, \dots, x_D]$ and observation y; a first-order Sobol' index $S_{1,d}$ for a particular parameter x_d ($d = 1, 2, \dots, D$) is defined by:

$$S_{1,d} = \frac{Var(E(y|x_d))}{Var(y)} = \frac{D_d}{D}. \qquad (6)$$

A second-order Sobol' index between input indices d and s shows the interaction between x_d and x_s as follows:

$$S_{2,ds} = \frac{Var(E(y|x_d, x_s)) - Var(E(y|x_d)) - Var(E(y|x_s))}{Var(y)} = \frac{D_{ds}}{D}. \qquad (7)$$

To express the whole effect of the input on the output, the total Sobol' index S_T can be obtained as follows:

$$S_{T,d} = S_{1,d} + \sum_{s \neq d}^{D} S_{2,ds} + \sum_{s \neq d, r \neq d, s < r}^{D} S_{3,dsr} + \cdots + S_D. \qquad (8)$$

Therefore, the first-order Sobol' indices measure the contribution to the variance solely attributable to x_d, whereas the total Sobol' index of d corresponds to its own contribution, including interactions with the other inputs.

As Sobol' indices are defined for scalar outputs, performing GSA on each output is insufficient because the correlations between them are unknown, which hinders the interpretation of the results. Therefore, the vector projection-based sensitivity indices (VPSIs) are used for the GSA of the multiple outputs [29]. For the multiple model outputs $\mathbf{y} = [y_1, y_2, \dots, y_N]$, the sensitivity indices are first defined by normalizing the multiple outputs to eliminate the interference of dimensions as follows:

$$\bar{y}_n = \frac{y_n}{\sigma(y_n)}, \quad n = 1, 2, \dots, N, \qquad (9)$$

where $\sigma(y_n) = \sqrt{Var(y_n)}$ denotes the standard deviation of y_n. The correlation coefficient matrix $\mathbf{R} = (r_{n_1,n_2})_{N \times N}$ of $\bar{y}_n$ is obtained to consider the correlations among the outputs, where $r_{n_1,n_2} = Cov(\bar{y}_{n_1}, \bar{y}_{n_2})$ with $n_1, n_2 = 1, 2, \dots, N$. The VPSIs are then expressed as follows:

$$P_{\Phi_i} = \frac{\mathbf{D}_{\Phi_i}^T \mathbf{R} \mathbf{D}}{\mathbf{D}^T \mathbf{R} \mathbf{D}}, \qquad (10)$$

where $\Phi_i = \{i_1, i_2, \dots, i_s\}$ is a set of integers with cardinality s, $\mathbf{D} = [D^{y_1}, D^{y_2}, \dots, D^{y_N}]^T$, $\mathbf{D}_{\Phi_i} = [D_{\Phi_i}^{y_1}, D_{\Phi_i}^{y_2}, \dots, D_{\Phi_i}^{y_N}]^T$, and $D^{y_n} = Var(E(y_n))$. The total VPSIs are then calculated by:

$$P_{T_i} = \sum_{i \in \Phi_k} P_{\Phi_k}, \qquad (11)$$

which represents the global sensitivity index of the ith parameter for multiple outputs. A polynomial chaos expansion (PCE) surrogate model was used in this study to calculate the VPSIs, following Sun et al. [29].

2.3. Model formulation

A lithium-ion cell consists of a positive electrode, negative electrode, and separator, as illustrated in Fig. 2. The P2D model is a physics-based model that describes the electrochemical properties based on the porous-electrode theory proposed by Doyle and Newman [8]. Assuming that the solid particles in the electrodes are spherical and symmetric, lithium concentration in each particle changes with time owing to the diffusion effect in the radial direction, as described by Fick's law:

$$\frac{\partial c_s}{\partial t} = \frac{D_s^{\text{eff}}}{r^2} \frac{\partial}{\partial r} \left(r^2 \frac{\partial c_s}{\partial r} \right), \qquad (12)$$

where c_s is the lithium concentration in a solid particle, t is the time, r is the radial direction of the particle, and D_s^{eff} is the effective diffusion coefficient in the solid phase. The boundary conditions can be described by the flux at the particle center and surface; its flux is zero at the center, and the surface flux is determined by electrode kinetics:

$$\left.\frac{\partial c_s}{\partial r}\right|_{r=0} = 0 \text{ and } \left.\frac{\partial c_s}{\partial r}\right|_{r=R_p} = -\frac{j}{D_s^{\text{eff}}}, \qquad (13)$$

where R_p is the particle radius and j is the pore wall flux of lithium-ion at the particle surface. To reduce the computational cost of solving the above equations for every grid, it is common to assume that the concentration distribution in a particle is quadratic in the radial direction [30]. Here, the average concentration (c_s^{avg}) is introduced, which is calculated by taking the volume average of the lithium concentration in a particle. Then, the difference between the surface concentration (c_{se}) and the average concentration can be obtained from the quadratic assumption.

$$\frac{\partial c_s^{\text{avg}}}{\partial t} = -3\frac{j}{R_p} \text{ and } c_{se} - c_s^{\text{avg}} = -\frac{R_p}{D_s^{\text{eff}}}\frac{j}{5}. \qquad (14)$$

Table 1
Governing equations and the boundary conditions of the P2D model.

Description	Domain	Governing equations	Boundary conditions
Mass conservation	Particle	$\frac{\partial c_s}{\partial t} = \frac{1}{r^2}\frac{\partial}{\partial r}\left(r^2 D_s^{\text{eff}}\frac{\partial c_s}{\partial r}\right)$ $\xrightarrow{\text{quad.dist.}} \frac{\partial c_{se}}{\partial t} = -\frac{3j}{R_p} - \frac{R_p}{5D_s^{\text{eff}}}\frac{\partial j}{\partial t}$	$\left.\frac{\partial c_s}{\partial r}\right|_0 = 0$ $\left.\frac{\partial c_s}{\partial r}\right|_{R_p} = -\frac{j}{D_s^{\text{eff}}}$
	Electrolyte	$\frac{\partial(\varepsilon_e c_e)}{\partial t} = \nabla\cdot(D_e^{\text{eff}}\nabla c_e) + a(1-t_+)j$	$\left.\frac{\partial c_e}{\partial x}\right|_{x_{ncc\|ne}}^{x_{pe\|pcc}} = 0$
Charge conservation	Electrode	$\nabla\cdot(\sigma^{\text{eff}}\nabla\phi_s) = aFj$	$\left.\sigma^{\text{eff}}\frac{\partial\phi_s}{\partial x}\right|_{x_{ncc\|ne}}^{x_{pe\|pcc}} = -I_{app}$ $\left.\sigma^{\text{eff}}\frac{\partial\phi_s}{\partial x}\right|_{x_{ne\|sep}}^{x_{sep\|pe}} = 0$
	Electrolyte	$\nabla\cdot\left[\kappa^{\text{eff}}\nabla\phi_e - \frac{2RT}{F}(1-t_+)\kappa^{\text{eff}}\nabla(\ln c_e)\right] = -aFj$	$\left.\phi_e\right|_{x_{ncc\|ne}} = 0$ $\left.\frac{\partial\phi_e}{\partial x}\right|_{x_{pe\|pcc}} = 0$
Electrode kinetics	Electrode	$j = 2k\sqrt{c_e\left(c_s^{\max}-c_{se}\right)c_{se}}\sinh\left(\frac{F}{2RT}\eta\right)$	
Energy balance	Cell	$\rho C_p\frac{\partial T}{\partial t} = \nabla\cdot(\lambda\nabla T) + Q_{ohm} + Q_{rev} + Q_{rxn}$	$\left.-\lambda\frac{\partial T}{\partial t}\right|_{x_{pcc}^{x_{ncc}}} = -h(T_{ref}-T)$

The lithium-ion concentration in the electrolyte is modeled by mass conservation. In the macroscopic model, only the diffusion effect and electrode kinetics are considered, while the migration and convection effects are neglected:

$$\varepsilon_e\frac{\partial c_e}{\partial t} = D_e^{\text{eff}}\frac{\partial^2 c_e}{\partial x^2} + a_s(1-t_+)j, \tag{15}$$

where ε_e is the porosity, c_e is the lithium concentration in the electrolyte, D_e^{eff} is the effective diffusivity in the electrolyte, a_s is the specific surface area of the active material, and t_+ is the transference number. In the separator domain, the second term on the right-hand side vanishes owing to the absence of the active material. The boundary conditions are described to satisfy the mass conservation. There is no net flux at the electrode/current collector interface, whereas the flux is conserved at the electrode/separator interface:

$$\left.\frac{\partial c_{e,i}}{\partial x}\right|_{ncc|ne} = 0, \quad \left.\frac{\partial c_{e,k}}{\partial x}\right|_{pe|pcc} = 0,$$
$$\left.\frac{\partial c_{e,i}}{\partial x}\right|_{ne|sep} = \left.\frac{\partial c_{e,j}}{\partial x}\right|_{ne|sep}, \quad\text{and}\quad i=ne,\ j=sep,\ k=pe, \tag{16}$$
$$\left.\frac{\partial c_{e,j}}{\partial x}\right|_{sep|pe} = \left.\frac{\partial c_{e,k}}{\partial x}\right|_{sep|pe}$$

where i, j, and k are the domain indices, and $|$ denotes the interface between domains. The solid-state potential at the electrodes is described by the charge conservation law, where the current density is derived from Ohm's law. Here, the electrode kinetics at the solid particle/electrolyte interface is the source and sink of the potential:

$$\nabla\cdot\mathbf{i}_{s,i} = \sigma_i^{\text{eff}}\frac{\partial^2\phi_{s,i}}{\partial x^2} = a_iFj_i, \qquad i=ne,pe, \tag{17}$$

where $\mathbf{i}_s$, σ^{eff}, and ϕ_s are the current density vector, the effective conductivity, and the electric potential in the solid phase, and F is the Faraday constant. The flux at the electrode/current collector interface is determined by the current applied to the cell, whereas the flux at the electrode/separator interface is zero:

$$\left.\sigma_i^{\text{eff}}\frac{\partial\phi_{s,i}}{\partial x}\right|_{ncc|ne} = -I_{app}, \quad \left.\sigma_j^{\text{eff}}\frac{\partial\phi_{s,j}}{\partial x}\right|_{pe|pcc} = -I_{app}, \quad i=ne,\ j=pe, \tag{18}$$
$$\left.\sigma_i^{\text{eff}}\frac{\partial\phi_{s,i}}{\partial x}\right|_{ne|sep} = 0, \text{ and } \left.\sigma_j^{\text{eff}}\frac{\partial\phi_{s,j}}{\partial x}\right|_{sep|pe} = 0$$

where I_{app} is the applied current density. The electrolyte potential is described by charge conservation. For the ionic current density, there exists one more term regarding the chemical potential compared to the solid phase:

$$\nabla\cdot(\varepsilon_{e,i}\mathbf{i}_{e,i}) = \kappa_i^{\text{eff}}\frac{\partial^2\phi_{e,i}}{\partial x^2} - \frac{2\kappa_i^{\text{eff}}RT}{F}(1-t_+)\frac{\partial^2\ln c_{e,i}}{\partial x^2} = \begin{cases} 0 & i=sep \\ -a_iFj_i & i=ne,pe, \end{cases} \tag{19}$$

where $\mathbf{i}_e$, κ^{eff}, and ϕ_e are the current density vector, the effective conductivity, and the electric potential in the electrolyte. The boundary conditions indicate that there is zero flux at the electrode/current collector interface and that the flux is continuous at the electrode/separator interface. However, a reference value of the electrolyte potential is required for a unique solution; thus, we set the electrolyte potential at the negative electrode/negative current collector boundary to zero:

$$\left.\phi_{e,i}\right|_{ncc|ne} = 0, \quad \left.\kappa_k^{\text{eff}}\frac{\partial\phi_{e,k}}{\partial x}\right|_{pe|pcc} = 0,$$
$$\left.\kappa_j^{\text{eff}}\frac{\partial\phi_{e,j}}{\partial x}\right|_{sep|pe} = \left.\kappa_k^{\text{eff}}\frac{\partial\phi_{e,k}}{\partial x}\right|_{sep|pe}, \quad\text{and}\quad i=ne,\ j=sep,\ k=pe. \tag{20}$$
$$\left.\kappa_i^{\text{eff}}\frac{\partial\phi_{e,i}}{\partial x}\right|_{ne|sep} = \left.\kappa_j^{\text{eff}}\frac{\partial\phi_{e,j}}{\partial x}\right|_{ne|sep}$$

The Butler–Volmer equation describes the electrode kinetics as follows:

$$j_i = k^{\text{eff}}\left[c_{e,i}\left(c_{s,i}^{\max}-c_{se,i}\right)\right]^{\alpha_a}\left[c_{se,i}\right]^{\alpha_c}$$
$$\times\left[\exp\left(\frac{\alpha_a F}{RT}\eta_i\right) - \exp\left(-\frac{\alpha_c F}{RT}\eta_i\right)\right] \quad i=ne,pe, \tag{21}$$

where k^{eff} is the effective reaction rate constant, α_a and α_c are the anodic and cathodic charge transfer coefficients, T is the temperature, and $\eta = \phi_s - \phi_e - U$ is the overpotential. For LIB cells, applying 0.5 to both α_a and α_c, the Butler–Volmer equation is simplified to:

$$j_i = 2k^{\text{eff}}\sqrt{c_{e,i}\left(c_{s,i}^{\max}-c_{se,i}\right)c_{se,i}}\sinh\left(\frac{F}{2RT}\eta_i\right) \quad i=ne,pe. \tag{22}$$

To reflect the thermal properties inside the LIB cell, we solve the energy balance equation considering heat sources such as ohmic (Q_{ohm}), reversible (Q_{rev}), and reaction (Q_{rxn}) heat generation:

$$\rho_i C_{p,i}\frac{\partial T_i}{\partial t} = \lambda_i\frac{\partial^2 T_i}{\partial x^2} + Q_{ohm,i} + Q_{rev,i} + Q_{rxn,i} \quad i=ncc,ne,sep,pe,pcc$$
$$Q_{ohm,i} = \sigma_i^{\text{eff}}\left(\frac{\partial\phi_{s,i}}{\partial x}\right)^2 + \kappa_i^{\text{eff}}\left(\frac{\partial\phi_{e,i}}{\partial x}\right)^2$$
$$\qquad - \kappa_i^{\text{eff}}\frac{2RT_i}{F}(1-t_+)\frac{\partial\ln c_{e,i}}{\partial x}\frac{\partial\phi_{e,i}}{\partial x} \quad i=ncc,ne,pe,pcc \quad , \tag{23}$$
$$Q_{rev,i} = a_iFj_iT_i\left.\frac{\partial U_i}{\partial T}\right|_{T_{ref}} \quad i=ne,pe$$
$$Q_{rxn,i} = a_iFj_iT_i\eta \quad i=ne,pe$$

where ρ is the density, C_p is the specific heat, and λ is the thermal conductivity. The heat exchange at the boundaries is modeled using the heat exchange coefficient h:

$$\left.-\lambda\frac{\partial T}{\partial x}\right|_{ncc,pcc} = -h(T_{ref}-T_{ncc,pcc}). \tag{24}$$

Table 2
Parameters used in the pseudo-two-dimensional model.

Parameter	Description	Unit
c_e^0	Initial concentration in the electrolyte[a]	mol m^{-3}
$c_{s,ne}^0$, $c_{s,pe}^0$	Initial solid-phase concentration[a]	mol m^{-3}
$c_{s,ne}^{\max}$, $c_{s,pe}^{\max}$	Maximum solid-phase concentration	mol m^{-3}
$D_{e,ne}$, $D_{e,sep}$, $D_{e,pe}$	Electrolyte diffusivity	$\text{m}^2\,\text{s}^{-1}$
$D_{s,ne}$, $D_{s,pe}$	Solid-phase diffusivity	$\text{m}^2\,\text{s}^{-1}$
k_{ne}, k_{pe}	Reaction rate constant[a]	$\text{m}^{2.5}\,\text{mol}^{-0.5}\,\text{s}^{-1}$
L_{ncc}, L_{ne}, L_{sep}, L_{pe}, L_{pcc}	Thickness	m
$R_{p,ne}$, $R_{p,pe}$	Particle radius[a]	m
ρ_{ncc}, ρ_{ne}, ρ_{sep}, ρ_{pe}, ρ_{pcc}	Density	kg m^{-1}
$C_{p,ncc}$, $C_{p,ne}$, $C_{p,sep}$, $C_{p,pe}$, $C_{p,pcc}$	Specific heat	$\text{J kg}^{-1}\,\text{K}^{-1}$
λ_{ncc}, λ_{ne}, λ_{sep}, λ_{pe}, λ_{pcc}	Thermal conductivity	$\text{W m}^{-1}\,\text{K}^{-1}$
σ_{ncc}, σ_{ne}, σ_{pe}, σ_{pcc}	Solid-phase conductivity	S m^{-1}
κ_{ne}, κ_{sep}, κ_{pe}	Electrolyte conductivity	S m^{-1}
$\varepsilon_{e,ne}$, $\varepsilon_{e,sep}$, $\varepsilon_{e,pe}$	Porosity[a]	–
$a_{s,ne}$, $a_{s,pe}$	Particle specific surface area[a]	m^{-1}
$E_{a,ne}^{D_s}$, $E_{a,pe}^{D_s}$	Solid-phase diffusion activation energy	J mol^{-1}
$E_{a,ne}^k$, $E_{a,pe}^k$	Reaction constant activation energy	J mol^{-1}
$brugg$	Bruggeman coefficient[a]	–
F	Faraday constant	C mol^{-1}
R	Universal gas constant	$\text{J mol}^{-1}\,\text{K}^{-1}$
t_+	Transference number	–
$\varepsilon_{s,ne}$, $\varepsilon_{s,pe}$	Filler fraction[a]	–

[a] Parameters to estimate in this study.

Table 3
Comparison of the present electrochemical model with LIONSIMBA [31] under different C-rates.

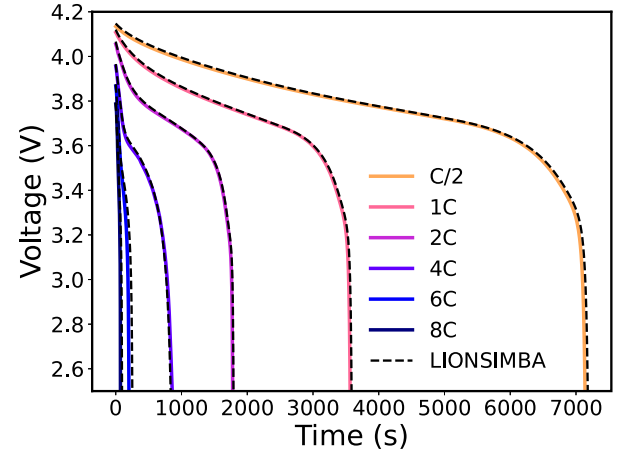| C-rate	Discharging time (s)	Computation time (s)		Mean absolute error (V)
		Present model	LIONSIMBA [31]	
C/2	7178	2.587	3.213	0.0093
1C	3586	2.507	2.849	0.0092
2C	1790	2.381	3.135	0.0092
4C	834	2.239	3.488	0.0195
6C	251	2.031	4.060	0.0881
8C	95	1.911	3.575	0.0704

Fig. 3. Voltage comparison of the present electrochemical model with LIONSIMBA [31] under different C-rates.

The value of the heat exchange coefficient used in our simulation was 0.01 W/(m²K). The above-governing equations and boundary conditions are summarized in Table 1, and additional open-circuit potential equations, dynamic coefficients, and reference parameters are obtained from Tables 2 and 4 in Torchio et al. [31]. For the dynamic coefficients, electrode-related parameters (D_s^{eff}, k^{eff}) are obtained from the Arrhenius equation, and the electrolyte-related parameters (D_e^{eff}, κ^{eff}) are calculated using the porosity and the Bruggeman coefficient ($brugg$) according to Bruggeman's theory.

3. Implementation details

Parameters related to the material of each electrode and the geometry of the LIB cell, such as open-circuit voltage and activation energy of each parameter, were excluded from the model parameters to be identified. In addition, parameters such as the maximum solid-phase concentration, density, specific heat, thermal conductivity, electrode area, and thickness have theoretical values or can be measured directly. Parameters such as the solid-phase diffusivity, transference number, and solid-phase conductivity show relatively lower sensitivity and can be corrected by other parameters, according to Xu et al. [17]. We included the remaining 15 parameters in the electrochemical model to be identified: the specific surface ($a_{s,pe}$, $a_{s,ne}$), solid particle radius ($R_{p,pe}$, $R_{p,ne}$), porosity ($\varepsilon_{e,pe}$, $\varepsilon_{e,sep}$, $\varepsilon_{e,ne}$), filler fraction ($\varepsilon_{s,pe}$, $\varepsilon_{s,ne}$), rate constant (k_{pe}, k_{ne}), Bruggeman coefficient ($brugg$), initial solid-phase concentration ($c_{se,pe}^0$, $c_{se,ne}^0$), and initial electrolyte concentration (c_e^0). It should be noted that the subscripts pe, sep, and ne indicate the positive electrode, separator, and negative electrode, respectively. Table 2 lists the P2D model parameters, where the symbol 'a' denotes the parameters to estimate in this study.

To calculate the likelihood of obtaining (1), the objective function in Bayesian PI is based on the weighted total least squares (WTLS) algorithm to minimize errors between the reference data and the model output [32]. The WTLS objective function can be written as:

$$F(\mathbf{x}; \mathbf{y}_{ref}) = \sum_{n=1}^{N} \left(\frac{(V_{ref,n} - V_{est,n}(\mathbf{x}))^2}{\sigma_v^2} + \frac{(t_{ref,n} - t_{est,n}(\mathbf{x}))^2}{\sigma_t^2} \right), \quad (25)$$

where N is the number of data points in the voltage curves, n indicates a point index, $V_{est,n}(\mathbf{x})$ and $t_{est,n}(\mathbf{x})$ are the estimated voltage and corresponding time, respectively, with a given parameter $\mathbf{x}$, $\mathbf{y}_{ref} = [V_{ref,1}, V_{ref,2}, \dots, V_{ref,N}, t_{ref,1}, t_{ref,2}, \dots, t_{ref,N}]$ is the reference voltage and corresponding time from the experiments, and σ_v^2 and σ_t^2 are the predefined variances for voltage and time, respectively. When only the voltage over time is minimized, the objective function of the model output that reaches the cut-off voltage faster than the reference voltage curve is calculated, ignoring a part of the reference voltage. Moreover, the objective function of the model output that reaches the cut-off voltage later than the reference voltage curve is calculated while ignoring a part of the estimated voltage. The WTLS is useful to solve these problems because, even if the output voltage curve of the model is longer or shorter than the reference voltage curve, all elements of the curve are used to obtain the objective function. Finally, using (25) as the objective function, the distribution of the parameters is derived from the voltage curve through MCMC with AIES. The MCMC with the AIES algorithm and global sensitivity analysis were implemented using the UQLab framework [33].

Below detailed procedure of Bayesian PI is listed.

1. Given a reference discharge voltage–time curve under a certain C-rate, the variances σ_v^2 and σ_t^2 are calculated to construct the objective function (25). It is worth noting that, when dividing the curve in equal lengths, the number of data points is set to $N = 20$.
2. As the electrochemical parameters are physically constrained to positive values, independent lognormal distributions are used for prior distributions of parameters. Assuming that prior knowledge of the parameter values is insufficient, the standard deviations of the lognormal distributions are set to 40% of each reference parameter value. Using the MCMC with AIES described in Section 2.1, the marginal and joint posterior distributions of

Table 4

Summary of reference parameters and maximum a posteriori (MAP) with 95% confidence interval (CI) of estimated distributions under C/2, 1C, and 4C. Note that R_{CI} represents the relative length of CI divided by the reference value.

Parameter	Unit	Reference value	C-rate	MAP	95% CI	R_{CI}
$a_{s,ne}$	$m^2\,m^{-3}$	723 600	C/2	743 313	[602 476, 868 795]	0.368
			1C	700 387	[567 361, 922 940]	0.491
			4C	658 420	[503 448, 1 136 288]	0.875
$a_{s,pe}$	$m^2\,m^{-3}$	885 000	C/2	885 535	[650 577, 1 118 711]	0.529
			1C	921 178	[703 959, 1 224 804]	0.589
			4C	772 257	[628 091, 1 139 380]	0.578
$R_{p,ne}$	m	2.000×10^{-6}	C/2	2.068×10^{-6}	$[1.799 \times 10^{-6}, 2.743 \times 10^{-6}]$	0.472
			1C	2.146×10^{-6}	$[1.642 \times 10^{-6}, 2.562 \times 10^{-6}]$	0.460
			4C	1.949×10^{-6}	$[1.323 \times 10^{-6}, 2.810 \times 10^{-6}]$	0.744
$R_{p,pe}$	m	2.000×10^{-6}	C/2	2.048×10^{-6}	$[1.582 \times 10^{-6}, 2.760 \times 10^{-6}]$	0.589
			1C	1.948×10^{-6}	$[1.434 \times 10^{-6}, 2.526 \times 10^{-6}]$	0.546
			4C	1.630×10^{-6}	$[1.223 \times 10^{-6}, 2.097 \times 10^{-6}]$	0.437
$\varepsilon_{e,ne}$	–	0.485	C/2	0.378	[0.260, 0.783]	1.079
			1C	0.396	[0.288, 0.762]	0.977
			4C	0.416	[0.304, 0.637]	0.687
$\varepsilon_{e,sep}$	–	0.724	C/2	0.554	[0.332, 1.304]	1.342
			1C	0.840	[0.429, 1.464]	1.429
			4C	0.697	[0.514, 1.041]	0.728
$\varepsilon_{e,pe}$	–	0.385	C/2	0.341	[0.193, 0.651]	1.190
			1C	0.271	[0.198, 0.507]	0.802
			4C	0.356	[0.232, 0.479]	0.640
$brugg$	–	4	C/2	3.376	[2.172, 5.938]	0.941
			1C	2.905	[2.310, 5.391]	0.770
			4C	3.333	[2.568, 4.750]	0.546
$c_{se,ne}^{0}$	$mol\,m^{-3}$	26 128	C/2	24 626	[20 231, 28 440]	0.314
			1C	25 176	[21 757, 29 518]	0.297
			4C	26 915	[18 523, 29 509]	0.421
$c_{se,pe}^{0}$	$mol\,m^{-3}$	25 751	C/2	25 500	[25 218, 26 068]	0.033
			1C	25 680	[25 099, 26 236]	0.044
			4C	25 993	[24 751, 26 809]	0.080
c_{e}^{0}	$mol\,m^{-3}$	1000	C/2	931	[515, 1804]	1.289
			1C	893	[600, 1602]	1.001
			4C	987	[749, 1399]	0.651
$\varepsilon_{s,ne}$	–	0.0326	C/2	0.0238	[0.0133, 0.0728]	1.826
			1C	0.0298	[0.0144, 0.0660]	1.581
			4C	0.0314	[0.0146, 0.0620]	1.455
$\varepsilon_{s,pe}$	–	0.0250	C/2	0.0169	[0.0115, 0.0483]	1.470
			1C	0.0172	[0.0108, 0.0443]	1.339
			4C	0.0268	[0.0139, 0.0411]	1.090
k_{ne}	$m^{2.5}\,mol^{-0.5}\,s^{-1}$	5.031×10^{-11}	C/2	4.040×10^{-11}	$[2.252 \times 10^{-11}, 1.022 \times 10^{-10}]$	1.583
			1C	4.984×10^{-11}	$[2.227 \times 10^{-11}, 9.223 \times 10^{-11}]$	1.391
			4C	5.435×10^{-11}	$[2.125 \times 10^{-11}, 8.154 \times 10^{-11}]$	1.198
k_{pe}	$m^{2.5}\,mol^{-0.5}\,s^{-1}$	2.334×10^{-11}	C/2	1.884×10^{-11}	$[1.106 \times 10^{-11}, 4.640 \times 10^{-11}]$	1.514
			1C	1.689×10^{-11}	$[1.067 \times 10^{-11}, 4.038 \times 10^{-11}]$	1.273
			4C	1.685×10^{-11}	$[1.096 \times 10^{-11}, 3.448 \times 10^{-11}]$	1.008

the parameters are obtained; the number of chains and steps are set to 100 and 10,000, respectively.

3. In practical MCMC applications, it is common to discard the sample points generated prior to the convergence of the chains, which is called *burn-in* [34]. By default, in UQLab, the first half of the sample points generated by all chains are removed. In addition, as some chains do not converge in the empirical distributions, half of the chains with the lowest acceptance rates are removed. Finally, the remaining 250,000 posterior samples for each parameter are used for UQ analysis.

4. Results and discussion

4.1. Electrochemical model validation

An accurate and fast model solver is required to identify the model parameters in a reasonable time because the Bayesian PI is based on a stochastic approach. Therefore, we developed an in-house P2D model solver and compared the results and performance with the Lithium-ION SIMulation BAttery (LIONSIMBA) toolbox [31], an open-source P2D model analysis software. Different constant-current discharges (C/2, 1C, 2C, 4C, 6C, and 8C) were simulated, and the results are shown in Fig. 3 and Table 3. In Fig. 3, the solid lines (our solver) show good agreement with the dashed lines (LIONSIMBA), particularly under a low C-rate. The mean absolute errors (MAEs) are shown in Table 3, where the MAE between the reference voltage $V_{ref}(t)$ and simulated voltage $V_{sim}(t)$ at time step $t = 1, 2, \ldots, T$ is defined as follows:

$$MAE = \frac{1}{T} \sum_{t=1}^{T} \left| V_{sim}(t) - V_{ref}(t) \right|. \tag{26}$$

At low C-rates (C/2, 1C, and 2C), the MAEs are approximately 10 mV, while high C-rates (4C, 6C, and 8C) show larger errors, which might have been caused by the numerical instability of our solver. We fully linearized the P2D model to solve it in a non-iterative manner, whereas the LIONSIMBA solved it using an iterative differential algebraic equation (DAE) solver. Nevertheless, our solver is suitable for evaluating the proposed PI method because of its computational performance. It
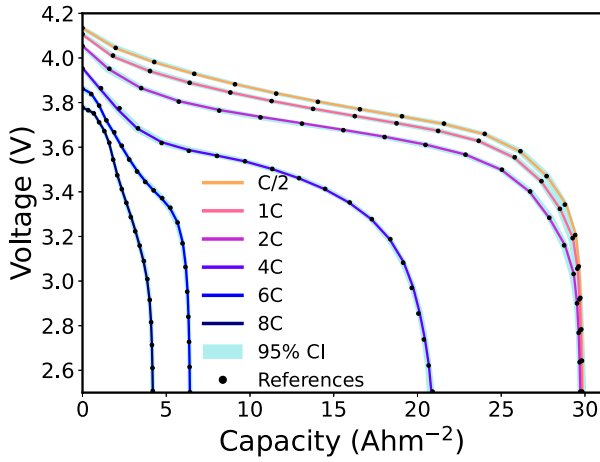
Fig. 4. Comparison of the estimated voltage with 95% confidence interval obtained from parameter distributions and reference voltage as a function of capacity per unit area under different C-rates.
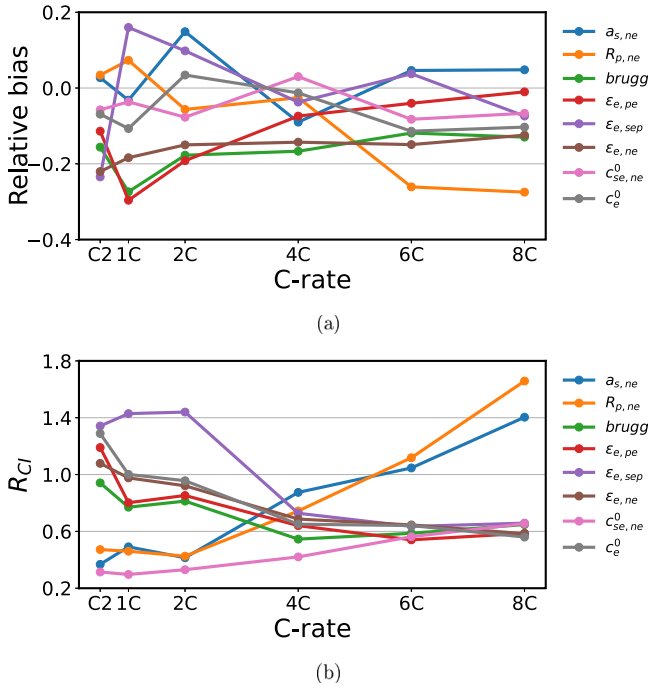

Fig. 5. Relative bias and relative length of 95% confidence interval (R_{CI}) of selected eight parameters for different C-rates.

solves the P2D model up to twice as fast as LIONSIMBA, especially at high C-rates.

It is worth noting that the role of the thermal model in this study is crucial, as it accounts for the temperature-dependent properties of certain parameters such as the open-circuit potential, solid-phase diffusivity, reaction rate constant, electrolyte diffusivity, and electrolyte conductivity, following Torchio et al. [31]. Different heat exchange coefficients for the thermal model boundary condition were tested, ranging from $h = 0.01$–$100\ \mathrm{W\,m^{-2}\,K^{-1}}$. At $h = 100\ \mathrm{W\,m^{-2}\,K^{-1}}$, the simulation results are similar to isothermal conditions, while at $h = 0.01\ \mathrm{W\,m^{-2}\,K^{-1}}$, the simulation approaches adiabatic conditions. Consequently, the temperature rises to approximately 298.3–366.9 K, which is in accordance with the heat exchange coefficients. Such increases in temperature are significant enough for the Arrhenius equation to adjust the effective parameters by approximately 46% at most, given an activation energy of $5000\ \mathrm{J\,mol^{-1}}$ as used in the simulations. Therefore,

the thermal properties were incorporated by adjusting the parameters according to the temperature increase due to heat sources.

4.2. Estimating parameter distributions

The marginal and joint posterior distributions of the electrochemical parameters were obtained using MCMC for different C-rates. To ensure that the parameter distributions were properly estimated through the MCMC, the reference voltages and voltages obtained through the P2D model with estimated parameter distributions were compared for various C-rates (C/2, 1C, 2C, 4C, 6C, and 8C). Fig. 4 illustrates the estimated voltage curves with 95% confidence intervals (CIs) compared with the reference target voltage. The solid lines for the estimated voltage were obtained using the MAP of the parameters, and the shaded areas for the 95% CIs were empirically obtained using sampled parameters from the estimated posterior distributions. Note that the discharge capacity C is defined as:

$$C = \frac{1}{3600} \int_0^{t_{end}} |I|\, dt, \tag{27}$$

where $|I|$ is the applied current, and t_{end} is the discharge end time. The relative errors between the estimated and reference voltages were 0.65%, 0.27%, 0.10%, 0.40%, 0.36%, and 0.15% for C/2, 1C, 2C, 4C, 6C, and 8C, respectively. The relative error is defined as $|V_{est} - V_{ref}|/V_{ref}$, where V_{est} and V_{ref} are the estimated and reference voltage curves, respectively. Moreover, the 95% CIs of the estimated voltages for all C-rates are narrow, indicating that the estimated parameter distributions were sufficiently reliable. For all C-rates, it is confirmed that the estimated and reference voltage curves show good agreement with relative errors, lower than 0.7%.

Table 4 lists reference parameters and estimated MAP with 95% CI of parameter distributions under C/2, 1C, and 4C. In addition, to investigate variations in the parameter distributions for different C-rates, the relative length of CI (R_{CI}) is defined as:

$$R_{CI} = \frac{x_U - x_L}{x_{ref}}, \tag{28}$$

where x_U and x_L are the upper and lower bounds of the 95% CI, respectively, and x_{ref} is the reference parameter. Overall, the estimated 95% CIs for all parameters and C-rates encompass the reference values, indicating that MCMC appropriately estimates the parameter distributions. For some parameters, R_{CI} and the differences between the reference values and MAPs change according to the C-rates. For example, for the specific surface in the negative electrode ($a_{s,ne}$), the MAPs are underestimated and the R_{CI} values increase as the C-rate increases. This indicates that the identifiability of $a_{s,ne}$ decreases when the C-rate increases, resulting in the estimated MAP being different from the reference value. However, for the specific surface in the positive electrode ($a_{s,pe}$), there are no significant changes in the estimated MAPs and R_{CI} values, indicating that $a_{s,pe}$ is less affected by the C-rate. The R_{CI} values of the filler fraction ($\varepsilon_{s,pe}$, $\varepsilon_{s,ne}$) and rate constant (k_{pe}, k_{ne}) exceed 1 for all C-rates, indicating that these parameters might be unidentifiable, regardless of the C-rates. In contrast, the R_{CI} values of the initial solid-phase concentration ($c_{se,pe}^0$, $c_{se,ne}^0$) are lower than those of the other parameters; in particular, the R_{CI} values of $c_{se,pe}^0$ for all C-rates are lower than 0.1, implying high identifiability of the parameters. A comparison of the proposed Bayesian PI with existing PI methods is provided in Appendix. This comparison further highlights the advantages of the proposed method in terms of estimating parameters and capturing uncertainties.

The relative bias between the reference values and the MAPs and R_{CI} of the selected parameters that showed meaningful changes for the different C-rates are illustrated in Fig. 5. Eight parameters were selected based on the significant changes in the R_{CI} according to the C-rate. Fig. 5(a) shows the relative bias of the parameters between the reference value x_{ref} and x_{MAP}, where the relative bias is defined as $(x_{MAP} - x_{ref})/x_{ref}$. Most parameter biases did not show a trend
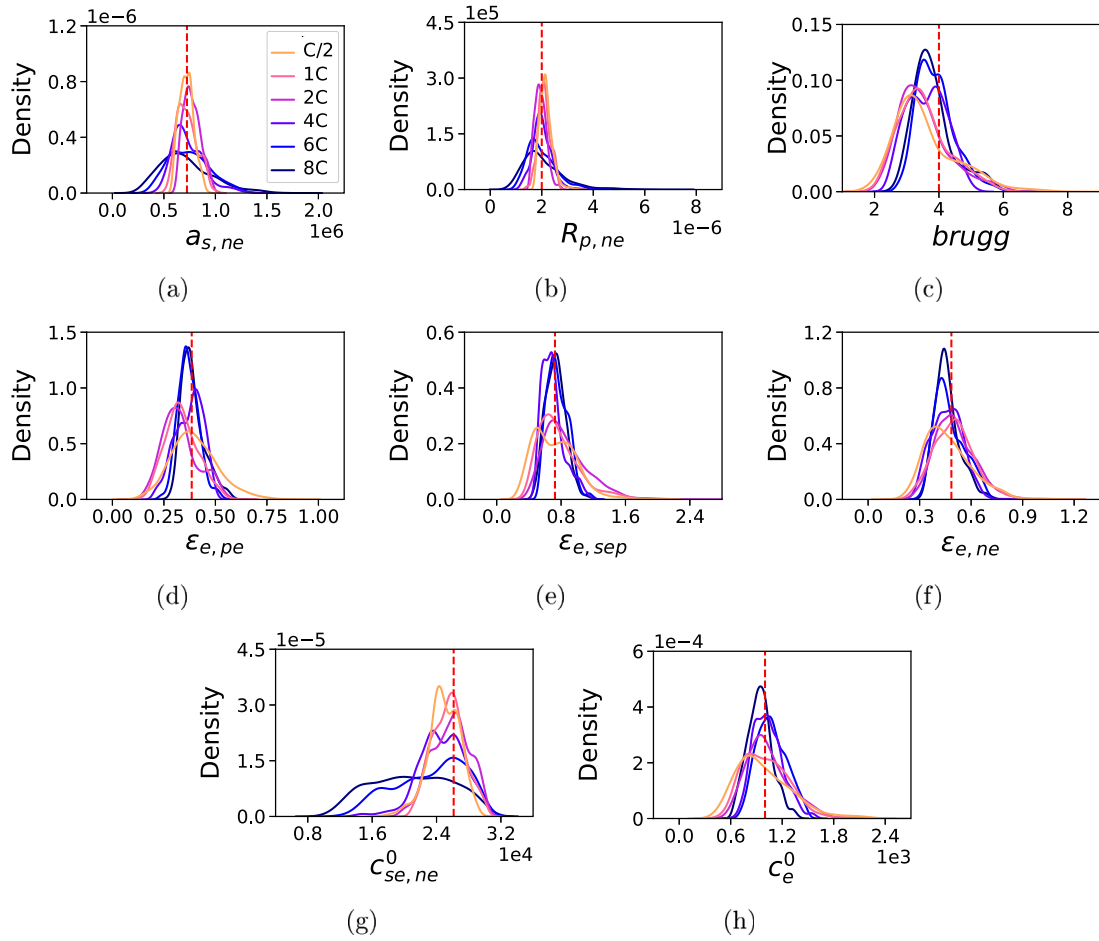
Fig. 6. Marginal posterior distribution of parameters for different C-rates.

according to the C-rate but maintained their values. However, in the case of $R_{p,ne}$, a negative bias appeared according to the C-rate, which is related to an increase in the R_{CI}. The changes in R_{CI} with respect to the C-rate are illustrated in Fig. 5(b). Unlike relative bias, changes in the R_{CI} show significant trends. For example, the R_{CI} values of $a_{s,ne}$, $R_{p,ne}$, and $c^0_{se,ne}$ increase as the C-rate increases, whereas those of ε_e, $brugg$, and c^0_e decrease.

To investigate the distributional changes in parameters for different C-rates, Fig. 6 illustrates the estimated distributions of the selected parameters shown in Fig. 5 according to the C-rate. Note that the red dotted line indicates the reference parameter values. As shown in Table 4, irrespective of the C-rate, the distributions of all parameters encompassed the reference values well. In particular, for the specific surface, particle radius, and initial solid-phase concentration in the negative electrode ($a_{s,ne}$, $R_{p,ne}$, $c^0_{se,ne}$), the dispersion of the distributions widened as the C-rate increased. Variations in the parameter distributions are related to identifiability, so $a_{s,ne}$, $R_{p,ne}$, and $c^0_{se,ne}$ may not be estimated under high C-rates. In contrast, the distributions of porosity ($\varepsilon_{e,pe}$, $\varepsilon_{e,sep}$, $\varepsilon_{e,ne}$), Bruggeman coefficient ($brugg$), and initial electrolyte concentration (c^0_e) became narrower as the C-rate increased. In other words, ε_e, $brugg$, and c^0_e may be unidentifiable at low C-rates.

Joint probability distributions for selected combinations are illustrated in Fig. 7 to analyze the correlations among the parameters. Four combinations of joint distributions were selected, among the 105 combinations among 15 parameters for different C-rates, corresponding to those where the absolute value of the Pearson correlation exceeds 0.8. Each row and column represent different combinations of the parameters and C-rates, respectively. The red stars indicate the reference values of the parameters, and the contour lines denote 20%, 40%, 60%,

and 80% levels of joint distributions. Overall, as shown in Fig. 7, the joint distributions also contain reference values for any C-rate. The first row represents the joint probability distributions between the particle radius and the specific surface in the positive electrode ($R_{p,pe}$, $a_{s,pe}$). It is confirmed that $R_{p,pe}$ and $a_{s,pe}$ are negatively correlated for all C-rates. This is because a_s can be represented in terms of R_p, assuming spherical particles, where $a_s = 3(1 - \varepsilon_e - \varepsilon_s)/R_p$. However, the correlation is alleviated as the C-rate increases, indicating that the spherical particle assumption might not be valid at high C-rates. On the other hand, three parameters, the Bruggeman coefficient ($brugg$) and the porosities in the electrodes ($\varepsilon_{e,pe}$, $\varepsilon_{e,ne}$), are positively correlated. The positive correlation is owing to tortuosity, which can be calculated as $\varepsilon_e^{1-brugg}$, where the correlations tend to increase as the C-rate increases.

4.3. Sensitivity analysis

VPSIs were calculated to quantitatively analyze the global sensitivity of the parameters for various C-rates, as illustrated in Fig. 8. Overall, the sensitivity indices of the parameters are inversely proportional to R_{CI}, as shown in Table 4. For example, the initial solid-phase concentration at the positive electrode ($c^0_{se,pe}$) has the smallest R_{CI}, whereas it has the largest VPSI, as shown in Fig. 8. On the other hand, VPSIs of the parameters with the largest variations, the filler fraction ($\varepsilon_{s,pe}$, $\varepsilon_{s,ne}$) and rate constant (k_{pe}, k_{ne}) are close to zero, indicating that these parameters have no significant effect on the voltage change. These results imply that the more sensitive the parameters, the narrower the distribution of the estimated parameters. Furthermore, the sensitivities of the correlated parameters, such as the specific surface (a_s) and particle radius (R_p), have similar trends. Similarly, as the
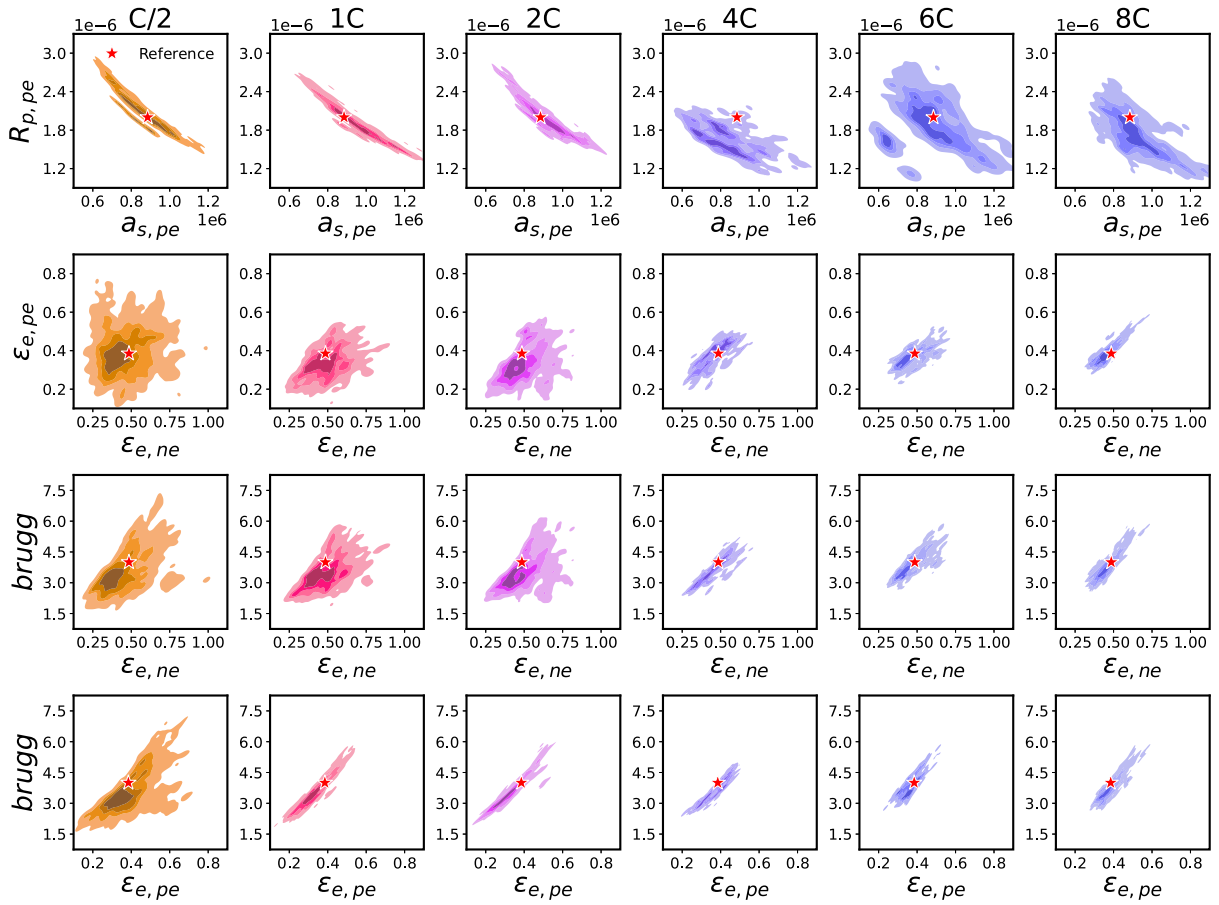
Fig. 7. Joint posterior distribution of parameters for different C-rates. The red star denotes the reference value of the parameters, and the contour lines denote 20%, 40%, 60%, and 80% levels of joint distributions.
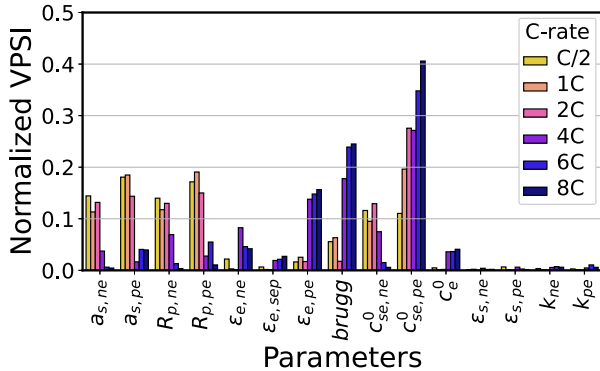

Fig. 8. Sobols' indices-based global sensitivity analysis for different C-rates.

The parameter interactions and their impact on the model output can be applied to refine the model structure and potentially reduce the number of parameters, which can simplify the model and make it more suitable for real-world applications. In particular, as reported in Streb et al. [35], the GSA can help guide the application of our proposed method in real-world settings by informing the selection of parameters to focus on during re-parametrization, depending on the specific usage patterns of the batteries.

5. Conclusions

This study presents a comprehensive framework for Bayesian PI to determine the posterior distributions of 15 parameters in a P2D model and the practical identifiability is quantitatively analyzed using variance-based global sensitivity analysis. Because the developed in-house P2D solver shows suitable computational performance, the distributions of several electrochemical parameters under various C-rates can be obtained using MCMC with AIES. As shown in Table 4, the estimated distributions encompass the reference values of the parameters, and the estimated MAPs of the parameters were close to the reference values for all C-rates. Using the estimated MAP of the parameters, the estimated and reference target voltage curves show good agreement with relative errors lower than 0.7% for all C-rates. Through the estimated joint and marginal distributions of the parameters, the practical identifiability of the parameters was investigated based on the relative length of CI (R_{CI}). In addition, using variance-based sensitivity analysis, the identifiability of the electrochemical parameters according to the discharge rates was quantitatively analyzed. The specific surface (a_s) and particle radius (R_p) in both electrodes and the

Bruggeman coefficient ($brugg$) and porosity in the electrodes ($\varepsilon_{e,ne}$, $\varepsilon_{e,pe}$) are correlated, as shown in Fig. 7, the sensitivities of these parameters increase at higher C-rates. Meanwhile, sensitivity varies for each parameter according to the C-rate. At low C-rates, a_s, R_p, and $c_{se,ne}^0$ are sensitive but become insensitive as the C-rate increases. In contrast, $brugg$, $\varepsilon_{e,pe}$, and $c_{se,pe}^0$ are more sensitive at high C-rates than at low C-rates. These results are related to R_{CI} in Table 4, where a lower R_{CI} implies a higher sensitivity, resulting in a higher identifiability [6]. In conclusion, a_s, R_p, and $c_{se,ne}^0$ are easy to identify at low C-rates, whereas $brugg$, $\varepsilon_{e,pe}$, and $c_{se,pe}^0$ are easy to identify at high C-rates. It is worth noting that the global sensitivity of the parameters can help to improve the model accuracy against real-world data under different conditions.
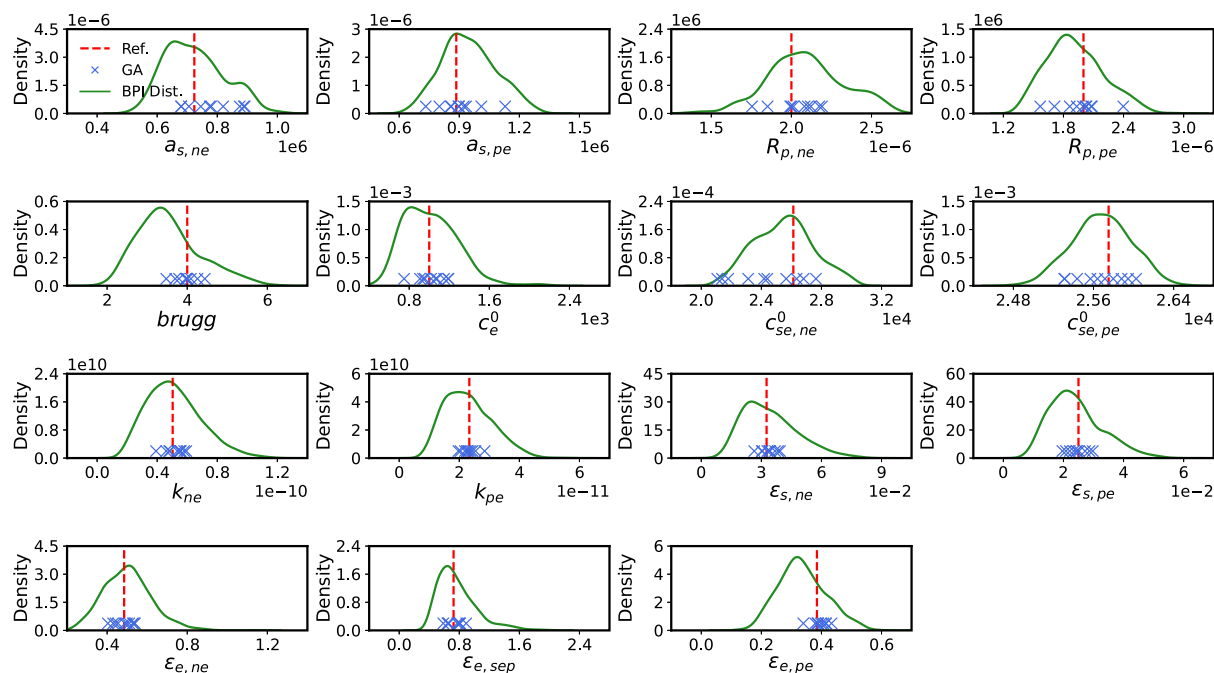
Fig. A.1. Marginal posterior distribution of parameters using Bayesian parameter identification (PI) and 10 estimated parameters using the genetic algorithm (GA). The red dotted line denotes the reference value of the parameters.

initial solid-phase concentration in the negative electrode ($c^0_{se,ne}$) were easy to identify under low C-rates, whereas the Bruggeman coefficient ($brugg$), porosity, and initial solid-phase concentration in the positive electrode ($\varepsilon_{e,pe}$, $c^0_{se,pe}$) were easy to identify under a high C-rate. The proposed framework not only serves as a calibration function that corrects the parameter values and their distributions for more accurate voltage predictions based on the P2D simulation results but also provides a comprehensive framework that accounts for parameter uncertainty, correlations, and identifiability. We demonstrate that the proposed Bayesian PI framework can help analyze the internal behavior of lithium-ion batteries and their performance according to specific operating conditions and materials, providing valuable insights for battery design and management.

CRediT authorship contribution statement

Seongyoon Kim: Conceptualization, Methodology, Software, Investigation, Visualization, Writing – original draft. **Sanghyun Kim:** Conceptualization, Methodology, Software, Investigation, Visualization, Writing – original draft. **Yun Young Choi:** Discussion. **Jung-Il Choi:** Conceptualization, Resources, Supervision, Writing – review & editing.

Declaration of competing interest

The authors declare that they have no known competing financial interests or personal relationships that could have appeared to influence the work reported in this paper.

Data availability

Data will be made available on request.

Acknowledgments

Appendix. Comparison of Bayesian parameter identification and genetic algorithm

A comparison between the proposed Bayesian parameter identification (PI) method and a widely used PI method, the genetic algorithm (GA), is provided. The comparison is performed using 1C discharge data for both methods. The estimated parameter distributions obtained through Bayesian PI and the parameter estimates from GA are shown in Fig. A.1. As GA is a stochastic PI method, we performed it 10 times to account for the variability in the results. The parameter estimates from the 10 GA iterations are plotted in Fig. A.1, where they are seen to lie well within the estimated parameter distributions obtained from the Bayesian PI method. Furthermore, the variation in the GA parameter estimates for the 10 iterations highlights the fact that the GA results may differ each time the algorithm is performed. In contrast, the Bayesian PI method effectively estimates both the parameters and their uncertainties, providing a more reliable and consistent parameter estimation compared to the stochastic GA method.

References

[1] M. Armand, J.-M. Tarascon, Building better batteries, Nature 451 (7179) (2008) 652–657.
[2] B. Dunn, H. Kamath, J.-M. Tarascon, Electrical energy storage for the grid: a battery of choices, Science 334 (6058) (2011) 928–935.
[3] K.-Y. Oh, N.A. Samad, Y. Kim, J.B. Siegel, A.G. Stefanopoulou, B.I. Epureanu, A novel phenomenological multi-physics model of Li-ion battery cells, J. Power Sources 326 (2016) 447–458.
[4] B. Liu, Y. Jia, C. Yuan, L. Wang, X. Gao, S. Yin, J. Xu, Safety issues and mechanisms of lithium-ion battery cell upon mechanical abusive loading: A review, Energy Storage Mater. 24 (2020) 85–112.
[5] X. Lai, C. Jin, W. Yi, X. Han, X. Feng, Y. Zheng, M. Ouyang, Mechanism, modeling, detection, and prevention of the internal short circuit in lithium-ion batteries: recent advances and perspectives, Energy Storage Mater. 35 (2021) 470–499.

[6] M. Andersson, M. Streb, J.Y. Ko, V.L. Klass, M. Klett, H. Ekström, M. Johansson, G. Lindbergh, Parametrization of physics-based battery models from input–output data: A review of methodology and current research, J. Power Sources 521 (2022) 230859.

[7] D. Zhang, S. Park, L.D. Couto, V. Viswanathan, S.J. Moura, Beyond battery state of charge estimation: Observer for electrode-level state and cyclable lithium with electrolyte dynamics, IEEE Trans. Transp. Electrif. (2022).

[8] M. Doyle, T.F. Fuller, J. Newman, Modeling of galvanostatic charge and discharge of the lithium/polymer/insertion cell, J. Electrochem. Soc. 140 (6) (1993) 1526.

[9] J.C. Forman, S.J. Moura, J.L. Stein, H.K. Fathy, Genetic identification and fisher identifiability analysis of the Doyle–Fuller–Newman model from experimental cycling of a LiFePO4 cell, J. Power Sources 210 (2012) 263–275.

[10] R. Xiong, L. Li, Z. Li, Q. Yu, H. Mu, An electrochemical model based degradation state identification method of Lithium-ion battery for all-climate electric vehicles application, Appl. Energy 219 (2018) 264–275.

[11] Z. Khalik, M. Donkers, J. Sturm, H.J. Bergveld, Parameter estimation of the doyle–fuller–newman model for Lithium-ion batteries by parameter normalization, grouping, and sensitivity analysis, J. Power Sources 499 (2021) 229901.

[12] E. Miguel, G.L. Plett, M.S. Trimboli, L. Oca, U. Iraola, E. Bekaert, Review of computational parameter estimation methods for electrochemical models, J. Energy Storage 44 (2021) 103388.

[13] X. Hu, S. Li, H. Peng, A comparative study of equivalent circuit models for Li-ion batteries, J. Power Sources 198 (2012) 359–367.

[14] W.-J. Lin, K.-C. Chen, Evolution of parameters in the Doyle-Fuller-Newman model of cycling lithium ion batteries by multi-objective optimization, Appl. Energy 314 (2022) 118925.

[15] Y.Y. Choi, S. Kim, K. Kim, S. Kim, J.-I. Choi, Parameter identification and identifiability analysis of lithium-ion batteries, Energy Sci. Eng. 10 (2) (2022) 488–506.

[16] W. Li, I. Demir, D. Cao, D. Jöst, F. Ringbeck, M. Junker, D.U. Sauer, Data-driven systematic parameter identification of an electrochemical model for lithium-ion batteries with artificial intelligence, Energy Storage Mater. 44 (2022) 557–570.

[17] L. Xu, X. Lin, Y. Xie, X. Hu, Enabling high-fidelity electrochemical P2D modeling of lithium-ion batteries via fast and non-destructive parameter identification, Energy Storage Mater. 45 (2022) 952–968.

[18] M. Sitterly, G.G. Yin, C. Wang, et al., Enhanced identification of battery models for real-time battery management, IEEE Trans. Sustain. Energy 2 (3) (2011) 300–308.

[19] H. Chun, K. Yoon, J. Kim, S. Han, Improving aging identifiability of lithium-ion batteries using deep reinforcement learning, IEEE Trans. Transp. Electrif. (2022).

[20] J.M. Escalante, S. Sahu, J.M. Foster, B. Protas, On uncertainty quantification in the parametrization of Newman-Type models of Lithium-Ion batteries, J. Electrochem. Soc. 168 (11) (2021) 110519.

[21] V. Ramadesigan, K. Chen, N.A. Burns, V. Boovaragavan, R.D. Braatz, V.R. Subramanian, Parameter estimation and capacity fade analysis of lithium-ion batteries using reformulated models, J. Electrochem. Soc. 158 (9) (2011) A1048.

[22] P. Tagade, K.S. Hariharan, S. Basu, M.K.S. Verma, S.M. Kolake, T. Song, D. Oh, T. Yeo, S. Doo, Bayesian calibration for electrochemical thermal model of lithium-ion cells, J. Power Sources 320 (2016) 296–309.

[23] M.D. Berliner, H. Zhao, S. Das, M. Forsuelo, B. Jiang, W.H. Chueh, M.Z. Bazant, R.D. Braatz, Nonlinear identifiability analysis of the porous electrode theory model of Lithium-Ion batteries, J. Electrochem. Soc. 168 (9) (2021) 090546.

[24] C. Andrieu, J. Thoms, A tutorial on adaptive MCMC, Stat. Comput. 18 (4) (2008) 343–373.

[25] J. Goodman, J. Weare, Ensemble samplers with affine invariance, Commun. Appl. Math. Comput. Sci. 5 (1) (2010) 65–80.

[26] C. Robert, G. Casella, Monte Carlo Statistical Methods, Springer Science & Business Media, 2013.

[27] J.V. Beck, K.J. Arnold, Parameter Estimation in Engineering and Science, James Beck, 1977.

[28] R.C. Smith, Uncertainty Quantification: Theory, Implementation, and Applications, Vol. 12, Siam, 2013.

[29] X. Sun, Y.Y. Choi, J.-I. Choi, Global sensitivity analysis for multivariate outputs using polynomial chaos-based surrogate models, Appl. Math. Model. 82 (2020) 867–887.

[30] V.R. Subramanian, V.D. Diwakar, D. Tapriyal, Efficient macro-micro scale coupled modeling of batteries, J. Electrochem. Soc. 152 (10) (2005) A2002.

[31] M. Torchio, L. Magni, R.B. Gopaluni, R.D. Braatz, D.M. Raimondo, Lionsimba: a matlab framework based on a finite volume model suitable for li-ion battery design, simulation, and control, J. Electrochem. Soc. 163 (7) (2016) A1192.

[32] G.L. Plett, Recursive approximate weighted total least squares estimation of battery cell total capacity, J. Power Sources 196 (4) (2011) 2319–2331.

[33] S. Marelli, B. Sudret, Uqlab: A framework for uncertainty quantification in matlab, in: Vulnerability, Uncertainty, and Risk: Quantification, Mitigation, and Management, 2014, pp. 2554–2563.

[34] S. Brooks, A. Gelman, G. Jones, X.-L. Meng, Handbook of Markov Chain Monte Carlo, CRC Press, 2011.

[35] M. Streb, M. Andersson, V.L. Klass, M. Klett, M. Johansson, G. Lindbergh, Investigating re-parametrization of electrochemical model-based battery management using real-world driving data, ETransportation 16 (2023) 100231.